

Observation of kagome-like bands in two-dimensional semiconducting $\text{Cr}_8\text{Se}_{12}$

Received: 2 November 2023

Accepted: 7 October 2024

Published online: 16 October 2024

Check for updates

Sisheng Duan^{1,2,10}, Jing-Yang You^{1,10}, Zhihao Cai^{3,10}, Jian Gou^{4,10} , Dong Li³, Yu Li Huang⁵, Xiaojiang Yu⁶, Siew Lang Teo⁷, Shuo Sun^{1,8}, Yihe Wang^{2,5}, Ming Lin⁷ , Chun Zhang¹, Baojie Feng³ , Andrew T. S. Wee¹ & Wei Chen^{1,2,5,9}

The kagome lattice is a versatile platform for investigating correlated electronic states. However, its realization in two-dimensional (2D) semiconductors for tunable device applications is still challenging. An alternative strategy to create kagome-like bands is to realize a coloring-triangle (CT) lattice in semiconductors through a distortion of a modified triangular lattice. Here, we report the observation of low-energy kagome-like bands in a semiconducting 2D transition metal chalcogenide— $\text{Cr}_8\text{Se}_{12}$ with a thickness of 7 atomic layers—which exhibits a CT lattice and a bandgap of 0.8 eV. The Cr-deficient layer beneath the topmost Se-full layer is partially occupied with $2/3$ occupancy, yielding a $\sqrt{3} \times \sqrt{3}$ Cr honeycomb network. Angle-resolved photoemission spectroscopy measurements and first-principles investigations reveal the surface kagome-like bands near the valence band maximum, which are attributed to topmost Se p_z orbitals modulated by the honeycomb Cr.

Both lattice geometry and dimension could profoundly shape the electronic structures of materials. Lattices with unique geometric configurations, including the kagome lattice^{1,2}, Lieb lattice^{3,4}, etc, exhibit correlated electronic excitations characterized by quenched kinetic energy of carriers in the flat band. Notably, diverse correlated phases, such as the giant anomalous Hall effect^{5–7}, quantum spin liquid^{8–11}, charge density wave^{12–15}, and unconventional superconductivity^{16–18}, have been observed in bulk kagome metals. Nonetheless, introducing these lattice-borne correlated excitations to 2D semiconductors, essential for device applications due to enhanced Coulomb interaction and versatile carrier concentration tunability, remains challenging.

The kagome lattice, comprised of corner-sharing triangles (Fig. 1a), represents a prototypical model for generating flat bands or

van Hove singularities (VHSs). However, experimental confirmation of kagome bands in 2D materials has been limited due to the instability of kagome configuration in two dimensions. Thus, alternatives such as the distorted kagome lattice (Fig. 1b) and the coloring-triangle (CT) lattice (Fig. 1c) have been proposed^{19,20} to exhibit a relatively rigid lattice and preserve the kagome bands. Both ways arise from rotating two sets of corner-sharing triangles within the kagome lattice. The CT lattice involves three types of hopping parameters, where t_1 and t_1' are ideally identical, and t_2 is zero. Its Hamiltonian is unitarily equivalent to that of the kagome lattice. Consequently, the band structures of the CT lattice also display a VHS, flat band and Dirac cone^{20,21}, as demonstrated in Fig. 1d. Even with slightly increased nonvanishing t_2 , the key features remain, except when t_2 becomes comparable to or exceeds t_1 (t_1'),

¹Department of Physics, National University of Singapore, 2 Science Drive 3, Singapore, Singapore. ²Department of Chemistry, National University of Singapore, 3 Science Drive 3, Singapore, Singapore. ³Institute of Physics, Chinese Academy of Sciences, Beijing 100190, China; School of Physical Sciences, University of Chinese Academy of Sciences, Beijing, China. ⁴School of Physics, Zhejiang University, Hangzhou, China. ⁵Joint School of National University of Singapore and Tianjin University, International Campus of Tianjin University, Binhai New City, Fuzhou, China. ⁶Singapore Synchrotron Light Source, National University of Singapore, 5 Research Link, Singapore, Singapore. ⁷Institute of Materials Research and Engineering (IMRE), A*STAR (Agency for Science, Technology and Research), 2 Fusionopolis Way, Singapore, Singapore. ⁸Department of Physics, Shanghai Key Laboratory of High Temperature Superconductors, Shanghai University, Shanghai, China. ⁹National University of Singapore (Suzhou) Research Institute, Suzhou, China. ¹⁰These authors contributed equally: Sisheng Duan, Jing-Yang You, Zhihao Cai, Jian Gou. e-mail: gouj@zju.edu.cn; m-lin@imre.a-star.edu.sg; bjfeng@iphy.ac.cn; phyweets@nus.edu.sg; phycw@nus.edu.sg

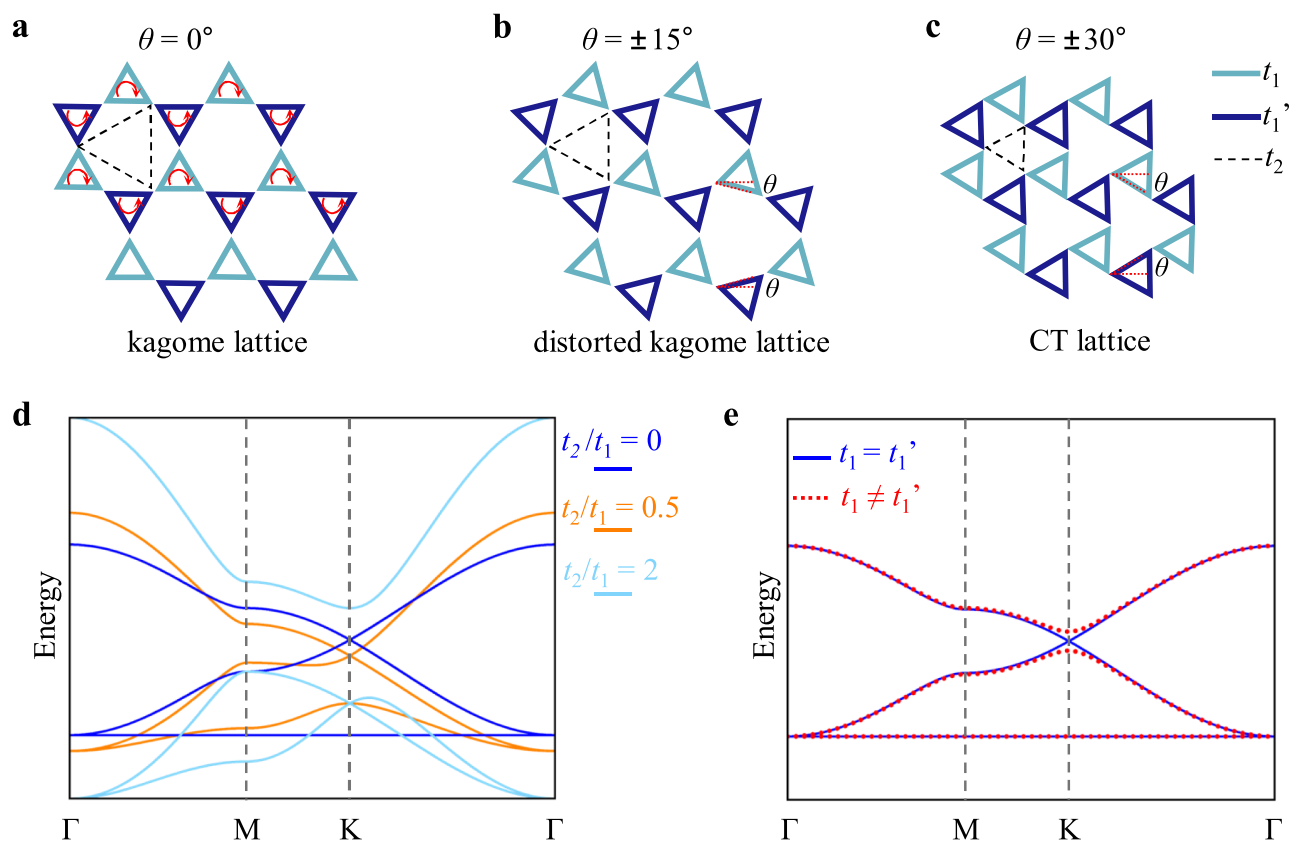


Fig. 1 | Illustration of the CT lattice band structures. **a, b, c** Schematic diagrams of the (a) kagome lattice, (b) distorted kagome lattice, and (c) CT lattice, which illustrate the evolution of the CT lattice from the unitary equivalent kagome lattice via rotating the corner-sharing triangles (θ). Three sets of hopping parameters,

namely t_1 , t_1' , and t_2 , are denoted by different colors. **d** Evolution of the CT lattice band structures with $t_1 = t_1'$, but the hopping parameter t_2 tuned from $t_2 = 0$ to $t_2 = 2$. **e** The CT lattice band structures that keep (blue, $t_1 = t_1'$) or break (red, $t_1 \neq t_1'$) the mirror symmetry.

leading to noticeable deviations from the archetypal kagome bands. The breaking of mirror symmetry ($t_1 \neq t_1'$) as shown in Fig. 1e only makes the Dirac cone massive, while the VHS and flat band persist in the band structures.

Various material platforms have been proposed theoretically to achieve the CT lattice, such as Au patterned Ca_2N^{20} , monolayer $\text{B}_2\text{S}_3^{22}$, Cu-dicyanobenzene²³, etc. However, none of these proposals have been materialized yet. Some experimental efforts have been paid to investigating the CT lattice in monolayer MoTe_2 and bulk 1T- $\text{TaS}_2^{24,25}$. Nonetheless, the complexity arises in these materials as each superlattice site consists of an atomic cluster containing several atoms, leading to intricate electronic structures. Hence, the development of 2D materials with atoms arranged on a CT lattice remains limited.

Herein, we report the molecular beam epitaxy (MBE) synthesis of semiconducting 2D $\text{Cr}_3\text{Se}_{12}$ with 7-atomic-layer thickness. Structural characterization shows that the atom-based CT lattice can be obtained by forming two atomic adlayers (Se-Cr) on the previously reported 5-atomic-layer Cr_2Se_3 . Based on the scanning tunneling spectroscopy (STS) and angle-resolved photoemission spectroscopy (ARPES) investigations, a bandgap of about 0.80 eV and a VHS close to the VBM (Supplementary Fig. 10) are observed. The first-principles analysis reveals that the kagome-like bands residing in the CT lattice originate from the top-layer Se p_z orbitals with alternative hopping parameters modulated by the underneath Cr honeycomb. The semiconducting nature and the divergent local density of states (LDOS) around the VBM render this material a promising candidate for investigating 2D strongly correlated physics in semiconducting devices.

Results

Crystal structures of 2D semiconducting $\text{Cr}_3\text{Se}_{12}$

The crystal structures of 2D chromium selenides including CrSe^{26} , $\text{CrSe}_2^{27,28}$, and $\text{Cr}_2\text{Se}_3^{28,29}$, are influenced by the synthesis methods and conditions. Here, the 2D chromium selenide was synthesized on graphite via MBE (see “Methods”, Supplementary Fig. 20 and Supplementary Fig. 22). A typical large-scale scanning tunneling microscopy (STM) topography of the as-grown chromium selenide is displayed in Fig. 2a, in which two types of terraces with different thicknesses are observable. The STM line profile (Fig. 2a, inset), taken along the orange dashed line, reveals the typical thicknesses of 1.03 nm and 1.30 nm, respectively. Based on detailed structure characterizations (Supplementary Note 1, Supplementary Fig. 1), we determined that the thinner phase with a lateral lattice constant $|\mathbf{a}_0| = 0.370 \pm 0.003$ nm is the previously reported “2D Cr_2Se_3 ”. This phase has a 5-atomic-layer thickness²⁸ and is composed of alternating stacks of Se-full and Cr-full layers along the (001) direction.

As for the thicker phase, structural analysis was conducted by examining the surface lattice arrangements of the two phases at the interface. Figure 2c, d present the STM and non-contact atomic force microscopy (nc-AFM) images obtained at the same scanning window, from which the surface lattice arrangements of thinner and thicker phases can be visualized simultaneously. Comparison of the surface Se triangle lattices of the thinner (upper) and thicker (lower) halves, represented by blue and red circles (Fig. 2d), reveals identical crystalline orientation and commensurate lattice constants between the two phases. The low energy electron diffraction (LEED) pattern in Fig. 2b, obtained from the sample incorporating both phases,

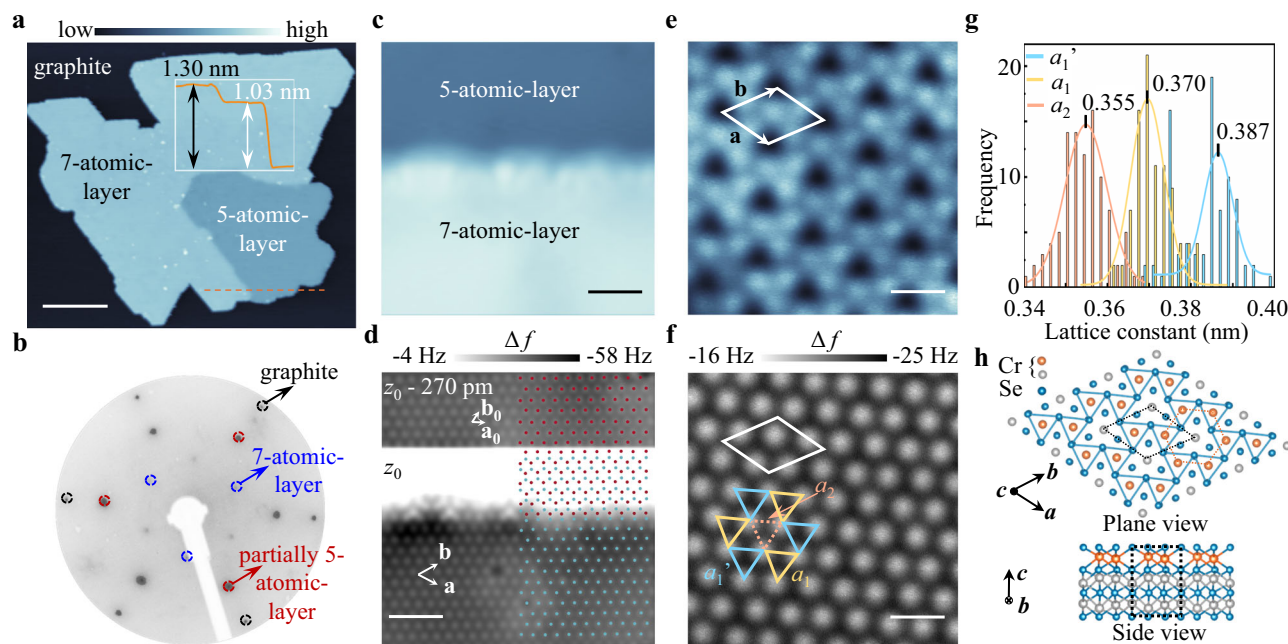


Fig. 2 | Crystal structure characterization of 2D $\text{Cr}_8\text{Se}_{12}$ on graphite. **a** STM topography ($V_s = 2\text{ V}$, $I = 5\text{ pA}$) of the chromium selenide sample with an orange dashed line across the 5-atomic-layer Cr_2Se_3 and 7-atomic-layer $\text{Cr}_8\text{Se}_{12}$. Inset: STM line profile along the orange dashed line. Scale bar: 15 nm. **b** LEED pattern of the as-grown chromium selenide sample on graphite. The black, red, and blue circles denote diffraction patterns from the graphite, 2D Cr_2Se_3 , and 2D $\text{Cr}_8\text{Se}_{12}$, respectively. **c, d** STM (**c**) and nc-AFM (**d**) images of the interface region acquired at the same scanning window. The lattice of 2D $\text{Cr}_8\text{Se}_{12}$ (2D Cr_2Se_3) is represented by the blue (red) circles. The primitive lattice vectors of 2D $\text{Cr}_8\text{Se}_{12}$ (2D Cr_2Se_3) are denoted by **a** and **b** (**a₀** and **b₀**), respectively. Imaging conditions for Fig. 2c: $V_s = 1.6\text{ V}$, $I = 100\text{ pA}$. Imaging conditions for the lower (upper) part of Fig. 2d:

$z_0 = -200\text{ pm}$ ($z_1 = -470\text{ pm} = z_0 - 270\text{ pm}$) relative to $V_s = 0.3\text{ V}$, $I = 100\text{ pA}$. Scale bars: 1.6 nm. **e, f** Atomic-resolved (**e**) constant height STM and (**f**) nc-AFM ($V_s = -0.01\text{ V}$, $z = -340\text{ pm}$ relative to $V_s = 0.3\text{ V}$, $I = 100\text{ pA}$) images of 2D $\text{Cr}_8\text{Se}_{12}$ obtained within the same scanning window, with the unit cell marked by the white rhombus and with different interatomic distances (a_1 , a_1' , and a_2) by triangles with diverse colors. Scale bars: 0.6 nm. **g** Statistical analysis of the measured nearest-neighbor interatomic distances: $a_1 = 0.370 \pm 0.005\text{ nm}$, $a_1' = 0.387 \pm 0.007\text{ nm}$ and $a_2 = 0.355 \pm 0.005\text{ nm}$. The distances were determined from Gaussian curve fitting of the histograms, with errors representing the standard deviations. **h** Crystal structures of 2D $\text{Cr}_8\text{Se}_{12}$ along different axes with the unit cell marked.

exhibits only one set of diffraction spots aligned with graphite. All these above witness a step-flow growth relation between the two phases. Further cross-sectional scanning transmission electron microscopy characterization (Supplementary Fig. 3) also suggests that thicker phase is formed through continuous epitaxial growth of additional Cr and Se layers on the 2D Cr_2Se_3 , resulting in a 7-atomic-layer crystal structure.

The atomic-resolved STM and nc-AFM images of the 7-atomic-layer phase, obtained within the same scanning window, are presented in Fig. 2e, f, respectively. Unlike STM, which relies on tunneling current for atomic-resolved imaging, nc-AFM utilizes short-range forces, allowing for a more precise determination of the real positions of surface Se atoms. A discernible $(\sqrt{3} \times \sqrt{3})R30^\circ$ surface reconstruction (depicted as the rhombuses in Fig. 2e and Supplementary Fig. 8) is easily identifiable. Statistical analysis indicates three distinct nearest-neighbor interatomic distances, denoted as a_1 , a_1' , and a_2 , within the $(\sqrt{3} \times \sqrt{3})R30^\circ$ unit cell (Fig. 2f, g). Notably, the periodic lattice distortion shapes the CT lattice geometrically. Indeed, the STM image displayed in Fig. 2e also exhibits a kagome-like morphology, indicating the potential of the thicker 7-atomic-layer phase for investigating the electronic properties of the kagome lattice.

To explain the $(\sqrt{3} \times \sqrt{3})R30^\circ$ surface reconstruction, we proposed three distinct crystal structures featuring 1/3, 2/3, and a full layer of Cr beneath the topmost Se (Supplementary Figs. 4a–c), corresponding to 1, 2, and 3 Cr atom(s) in the Cr adlayer per unit cell, respectively. Through density functional theory (DFT) calculations on their band structures (Supplementary Figs. 4d–f, Supplementary Fig. 5), we found that only the configuration with a 2/3-layer of Cr (Fig. 2h) exhibits a semiconducting behavior. Considering the experimentally determined semiconducting nature of the 7-atomic-layer phase (as discussed

later), we identify the crystal structure as the one with a 2/3-layer of Cr beneath the topmost Se (Fig. 2h). Notably, the 2/3-layer Cr atoms form a honeycomb network, linking the surface CT-lattice distortion to this honeycomb Cr arrangement. Given that each unit cell comprises 8 Cr atoms and 12 Se atoms (Supplementary Fig. 16), we henceforth denote the 7-atomic-layer phase as 2D $\text{Cr}_8\text{Se}_{12}$.

The crystal structure was further definitively elucidated through an analysis of its electronic properties using ARPES and DFT calculations. Figure 3a illustrates the $(\sqrt{3} \times \sqrt{3})R30^\circ$ commensurate relation between 2D $\text{Cr}_8\text{Se}_{12}$ and 2D Cr_2Se_3 , which causes an overlap of high-symmetry points between their respective Brillouin zones (BZs). The ARPES valence band dispersion in both BZs reveals their semiconducting nature (Fig. 3b). This is further demonstrated by the Fermi surface mapping (Fig. 3c), where only the π bands from the graphite substrate are observable. To identify band contributions, band structures of both phases were calculated (Fig. 3b) considering a small fraction of 2D Cr_2Se_3 in the $\text{Cr}_8\text{Se}_{12}$ sample used for ARPES measurements (Supplementary Fig. 2c). The superimposition of these band structures on the ARPES spectra demonstrates the agreement between theoretical calculations and experimental observations, corroborating the proposed crystal structures.

Band structure assignment also facilitates the exclusion of 2D Cr_2Se_3 during the analysis of 2D $\text{Cr}_8\text{Se}_{12}$ by comparing ARPES with localized STS characterizations. Specifically, the VBM revealed in dI/dV spectrum (Fig. 3e) closely aligns with the ARPES (Fig. 3b, Supplementary Fig. 9 and Supplementary Fig. 18) VBM, except for a slight downward shift attributable to the photohole doping that typically happens in semiconductors³⁰. A bandgap of -0.8 eV is observable in dI/dV spectrum, which is consistent with the absence of ARPES conduction band minimum until the Fermi level. Additionally, the LDOS (Fig. 3e

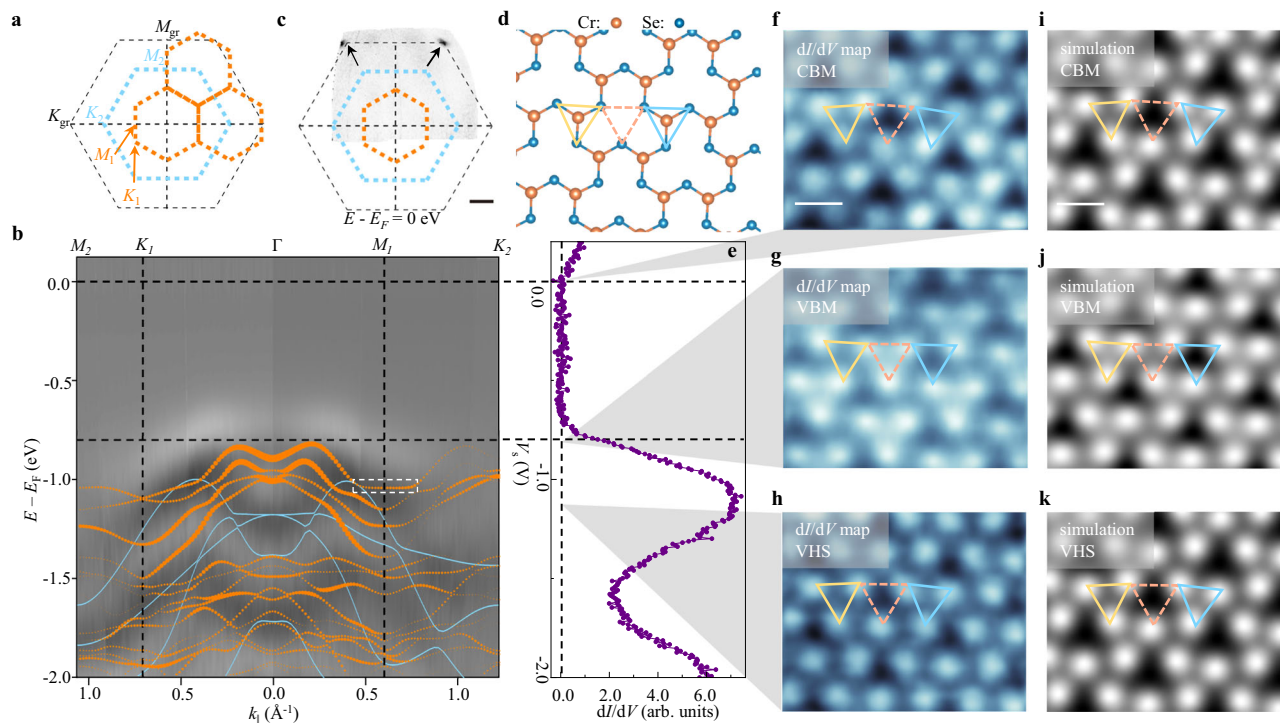


Fig. 3 | Electronic structures of 2D $\text{Cr}_8\text{Se}_{12}$ on graphite. **a** The geometric relation between the BZs of 2D $\text{Cr}_8\text{Se}_{12}$ (orange), 2D Cr_2Se_3 (blue), and the graphite substrate (black). **b** Second-derivative ARPES dispersion of the as-grown chromium selenide on graphite, which is measured at $T = 40$ K and displayed along the Γ - M_1 - K_2 and Γ - K_1 - M_2 directions as defined in Fig. 3a. The DFT band structure of 2D Cr_2Se_3 (blue, Supplementary Fig. 17) and unfolded band structure of 2D $\text{Cr}_8\text{Se}_{12}$ (orange, Supplementary Fig. 15) are superimposed for comparison with the ARPES data. The partial flat band near the M_1 point is marked by a white dashed rectangle. **c** Constant energy contour at Fermi level. Scale bar: 0.5 nm^{-1} . The Dirac cones of the graphite at Fermi level are marked by black arrows in Fig. 3c. **d** The schematic crystal structures

of the topmost two atomic adlayers for cross comparison with Fig. 3f-k. Three types of triangles are marked by different colors. **e** Energetically aligned dI/dV spectrum acquired on 2D $\text{Cr}_8\text{Se}_{12}$. ($V_s = 0.30 \text{ V}$, $I = 100 \text{ pA}$, $f = 963 \text{ Hz}$, $V_{r.m.s.} = 10 \text{ mV}$, $T = 4.3 \text{ K}$). **f-h** Constant-height dI/dV maps of 2D $\text{Cr}_8\text{Se}_{12}$ acquired at the same region and at energies corresponding to the (f) CBM ($V_s = 20 \text{ mV}$), (g) VBM ($V_s = -0.8 \text{ V}$), and (h) VHS ($V_s = -1.1 \text{ V}$), respectively. **i-k** DFT simulated charge density distributions of 2D $\text{Cr}_8\text{Se}_{12}$ acquired at energies corresponding to the (f) CBM, (g) VBM, and (h) VHS, respectively. Three types of triangles are marked by different colors as in panel (d).

and Supplementary Fig. 14) also manifests a pronounced valence peak centered at $V_s = -1.10 \text{ V}$, which is energetically aligned with a partial flat band near the M_1 point (Fig. 3b), i.e., the M point of 2D $\text{Cr}_8\text{Se}_{12}$.

The electronic structures including the VHS can be visualized in real space through dI/dV mapping within a specific region as illustrated in Fig. 3d. The dI/dV maps in Fig. 3f-h were measured at energies corresponding to the conduction band minimum (CBM), the VBM, and the VHS, respectively, which were reproduced by the DFT simulated charge density distributions at the corresponding energies (Fig. 3i-k). Notably, the mapping at VHS shows an electron localization at the Cr-bridged Se atoms, resulting in a kagome-like CT lattice pattern. Nevertheless, the LDOS distribution at the VBM presents the hexagonal close-packed trimers, corresponding to the parabolic band dispersion at the Γ point.

CT lattice-derived kagome-like bands in 2D $\text{Cr}_8\text{Se}_{12}$

While VHS and kagome-like morphology have been observed in 2D $\text{Cr}_8\text{Se}_{12}$, their exact origins remain elusive. We started from a careful analysis on the band structures of 2D $\text{Cr}_8\text{Se}_{12}$ through orbital projection. Figure 4a illustrates the spin-polarized band structure projected onto the p_z orbitals of the topmost Se atoms. Apparently, the energy states around the VBM, comprising six distinct energy bands, are primarily contributed by the topmost Se p_z orbitals (Supplementary Fig. 11 and Supplementary Fig. 19). These six energy bands can be categorized into two sets based on their spins: three are spin-up, and the remaining three are spin-down. Notably, within each unit cell of 2D $\text{Cr}_8\text{Se}_{12}$, three topmost Se atoms lead to the observation of six energy bands arising from two sets of CT lattice energy bands with distinct

spins. Consequently, the observed VHS contributed by the topmost Se p_z orbitals is supposed to originate from the CT lattice.

The kagome-like bands can be further reproduced through tight binding simulations. Given the semiconducting nature of 2D $\text{Cr}_8\text{Se}_{12}$, we employed the tight binding approximation without considering electron correlation effects (See Supplementary Information Part 10, Supplementary Fig. 24, Supplementary Fig. 25 for a discussion on electron correlation effects). The tight binding Hamiltonian was constructed on a CT lattice (Fig. 4b) with two distinct sets of nearest-neighbor hopping parameters. As displayed in Fig. 4c, the simulated band structures demonstrate qualitative agreement with the DFT band structures (Fig. 4a), with minor discrepancies that can be attributed to the neglected next-nearest-neighbor hopping and orbital mixing effect (see Supplementary Information Part 8, Supplementary Fig. 11 and Supplementary Fig. 12 for details).

The CT lattice may stem from a triangular lattice with periodically altered hopping parameters, resulting in exotic electronic excitations (Supplementary Fig. 13 and Supplementary Fig. 23). As demonstrated in Fig. 3d, within each unit cell of 2D $\text{Cr}_8\text{Se}_{12}$, the topmost Se atoms constitute the distorted triangle sublattice, while Cr atoms are located only below two of the three Se triangles. Since the bridging of Cr atoms tends to enhance the nearest-neighbor hopping between the Se atoms, the hopping within the Se triangles connected by bridging Cr atoms would surpass those without bridging, and this hopping configuration ($t_1 - t_1' > t_2$) benefits the formation of the kagome-like band structure in 2D $\text{Cr}_8\text{Se}_{12}$.

The CT lattice characteristics observed in the STM image (Fig. 2e) and dI/dV map (Fig. 3f) can be explained at the atomic scale.

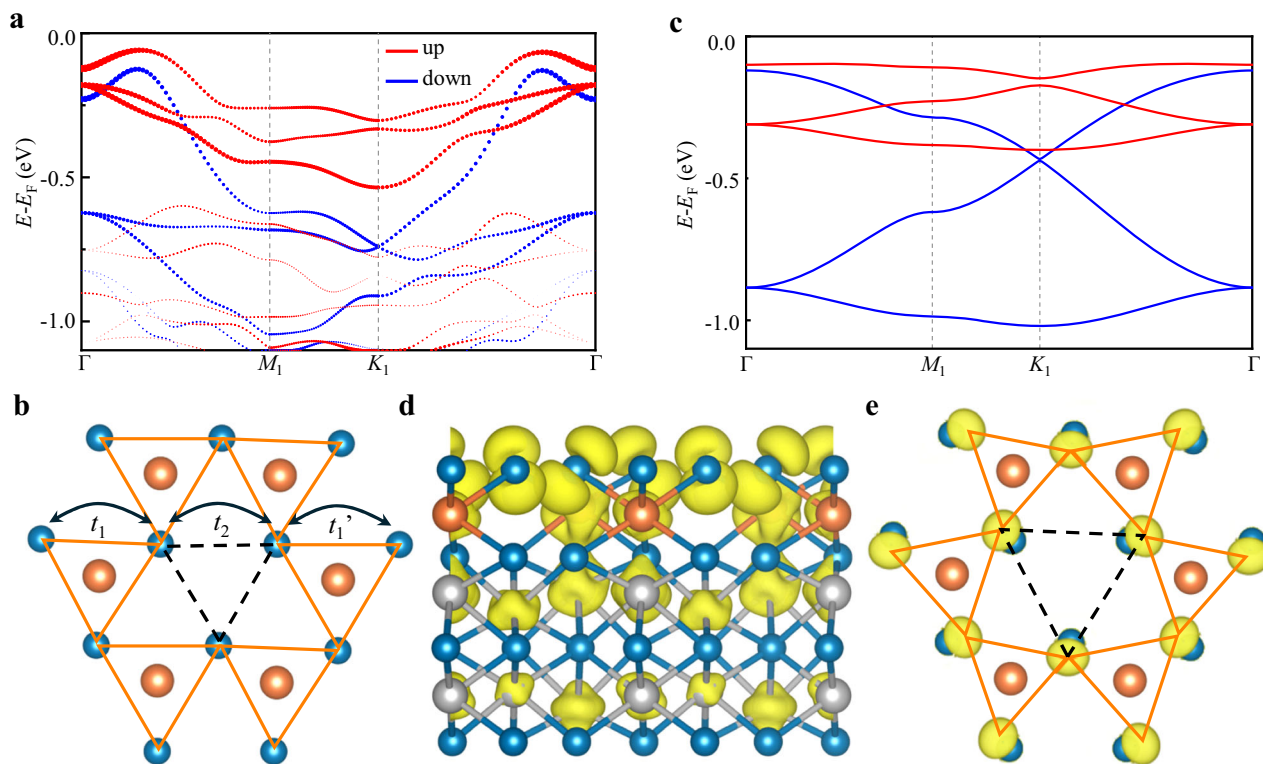


Fig. 4 | CT lattice in 2D $\text{Cr}_8\text{Se}_{12}$. **a** Spin-polarized DFT energy bands projected onto the top-layer Se p_z orbitals. **b** Tight binding model of the CT lattice on 2D $\text{Cr}_8\text{Se}_{12}$ with the three types of hopping parameters denoted by t_1 , t_1' , and t_2 . **c** Tight binding simulated energy bands showing qualitative agreement with the DFT band

structure. **d**, **e** Side (**d**) and top (**e**) views of the charge density distribution at the energy corresponding to the VHS. In Fig. 4e, only the topmost two atomic adlayers and the upper lobes of the Se orbitals are displayed.

Figure 4d displays a side view of the charge density distribution at the energy corresponding to the VHS, which not only verifies the major state contribution of the topmost Se p_z orbital at this energy, but clearly reveals the periodic tilt of these p_z orbitals. Thereafter, the Se p_z orbitals, as surface states, contribute the primary intensity to both the ARPES measurement and dI/dV map. Figure 4e presents the top-view spatial arrangements of the topmost Se p_z orbitals. By inspecting the tilt configurations, we found that the upper lobes of all the dumbbell-like p_z orbitals tend to tilt toward neighboring Cr atoms. Consequently, the triangular configuration of p_z orbitals contracts with the Cr in the middle, while expands in the absence of Cr at the center. This results in a prominent distortion of the triangular lattice and reproduces the observed dI/dV map with the CT lattice geometry. Additionally, the tilted orbitals at the atomic scale also substantiate the enhanced hopping $t_1(t_1')$ and the reduced hopping t_2 , thus resulting in the CT lattice-derived kagome-like bands.

Discussion

In summary, we have characterized the CT lattice in 2D $\text{Cr}_8\text{Se}_{12}$ with a 7-atomic-layer thickness, which is demonstrated to be a 2D semiconductor (See Supplementary Information part 4 and Supplementary Fig. 6 for discussion on the magnetic properties). The scalable synthesis of 2D $\text{Cr}_8\text{Se}_{12}$ not only expands the magnetic 2D materials family, but also opens a new avenue for investigating lattice-borne exotic electronic excitations. Notably, experimentally observed kagome-like bands originating from the CT lattice, accompanied by the prominently enhanced LDOS, were found near the VBM. This suggests a promising research direction involving the elevation of the VHS to the Fermi level, thereby enabling the observation of the proposed lattice-borne correlated phases.

Methods

Sample preparation

The 2D Cr_2Se_3 was grown in an ultra-high vacuum (UHV) MBE chamber with a base pressure of 1×10^{-10} mbar, which is connected to a commercial Omicron LT-STM/nc-AFM system. The cleaved single crystalline graphite (NGS Naturgraphit GmbH) or epitaxial graphene-terminated n-type 4H-SiC(0001) substrates have been used as the substrate. The graphite substrate was cleaved in air and immediately loaded into the MBE chamber to degas the surface contaminations. The epitaxial graphene was prepared by following the procedure demonstrated in ref. 31. High-purity Se (99.999%) and Cr (99.95%) were evaporated from a standard Knudson-style thermal effusion cell and an electron-beam evaporator, respectively, with a Se/Cr flux ratio higher than 10/1 and a substrate temperature of -440°C . The average growth rate for 2D $\text{Cr}_8\text{Se}_{12}$ is around 0.014 ML/minute.

STM/STS and nc-AFM measurements

For scanning probe microscopy characterizations, the as-grown Cr_2Se_3 samples were in-situ transferred into the Omicron LT-STM/nc-AFM system without breaking vacuum. The experiments were conducted at 4.3 K using a qPlus AFM sensor (spring constant $k_0 \approx 1800 \text{ N}\cdot\text{m}^{-1}$, resonance frequency $f_0 \approx 27.4 \text{ kHz}$, and quality factor $Q \approx 30,000$) equipped with a tungsten tip. The clean and atomically sharp tip apex was obtained by applying repeated voltage pulses and controllable crashes on the Au(111) substrate, and the tip state was calibrated on the Au(111) surface before the STS characterization. The STS spectra and dI/dV maps were acquired using standard lock-in technique with a bias modulation of 10 mV at 963 Hz. All the dI/dV maps were collected in the constant height mode. An oscillation amplitude of 40 pm is used for all the nc-AFM imaging. The STM and nc-AFM images were processed using the WSxM software.

ARPES measurements

ARPES experiments were conducted in UHV conditions at 40 K with a SPECS PHOIBUS 150 electron energy analyzer and a helium discharge lamp (He I_{α} light, $h\nu = 21.2$ eV). To prevent surface contamination, the Cr_2Se_3 samples were capped with ~ 10 nm of Se by deposition of Se at room temperature before being transferred to the ARPES system. Before the ARPES characterization, as shown in Supplementary Fig. 21, the Se capping layer was subsequently removed by annealing the samples at 300 °C for 30 minutes in UHV conditions (2.5×10^{-10} mbar).

First-principles calculations

Our first-principles calculations were based on DFT as implemented in the Vienna Ab Initio Simulation Package using the projector augmented-wave method. The generalized gradient approximation with the Perdew–Burke–Ernzerhof realization was adopted for the exchange–correlation functional. The plane-wave cutoff energy was set to 500 eV. A Monkhorst Pack k -point mesh with a size of $11 \times 11 \times 1$ was used for the BZ sampling. The crystal structure was optimized with the fixed experimental lattice constants and the fixed surface atom positions until the forces on the atoms were less than 0.001 eV/Å. To simulate the dI/dV maps, the partial charge density within an energy range of 0.02 eV centered at the specific energy was plotted as a function of the real space position.

Tight binding modeling

The spin polarized DFT analysis reveals that the major contributions to the six valence bands near the valence band maximum (VBM) are p_z orbitals of the topmost Se atoms. Three of them are spin-up bands and the other three are spin-down bands. In the absence of spin-orbit coupling, the spin and orbital parts of the electronic wave function are decoupled. Therefore, the spin polarized electrons in each spin channel can be treated separately like for spinless particles. We describe this behavior within a single-orbital tight binding model of connected p_z orbitals with two sets of hopping parameters, each of which corresponds to a set of spin-bands. By making a fit to the DFT spectra, we can determine the on-site energy ϵ_i and the hopping parameters t_i . With these parameters, we solve the generalized eigenvalue equation $H|\psi\rangle = E|\psi\rangle$ to obtain the tight binding spectra, where the spinless Hamiltonian is defined as $H = \sum_i \epsilon_i a_i^\dagger a_i + \sum_{\langle i,j \rangle} t_{nn}(a_i^\dagger a_j + a_i a_j^\dagger)$. Here, t_{nn} is the hopping parameter, which represents t_1 , t_1' or t_2 as defined in Fig. 4b.

Data availability

The authors declare that data generated in this study have been deposited in the FigShare database under accession code: <https://doi.org/10.6084/m9.figshare.26964691>.

Code availability

The authors declare that code supporting the findings of this study have been deposited in the FigShare database under accession code: <https://doi.org/10.6084/m9.figshare.26964691>.

References

- Kang, M. et al. Dirac fermions and flat bands in the ideal kagome metal FeSn. *Nat. Mater.* **19**, 163–169 (2020).
- Kang, M. et al. Topological flat bands in frustrated kagome lattice CoSn. *Nat. Commun.* **11**, 4004 (2020).
- Mukherjee, S. et al. Observation of a localized flat-band state in a photonic Lieb lattice. *Phys. Rev. Lett.* **114**, 245504 (2015).
- Slot, M. R. et al. Experimental realization and characterization of an electronic Lieb lattice. *Nat. Phys.* **13**, 672–676 (2017).
- Nakatsuji, S., Kiyohara, N. & Higo, T. Large anomalous hall effect in a non-collinear antiferromagnet at room temperature. *Nature* **527**, 212–215 (2015).
- Liu, E. et al. Giant anomalous hall effect in a ferromagnetic kagome-lattice semimetal. *Nat. Phys.* **14**, 1125–1131 (2018).
- Nayak, A. K. et al. Large anomalous hall effect driven by a non-vanishing berry curvature in the noncolinear antiferromagnet Mn_3Ge . *Sci. Adv.* **2**, e1501870 (2016).
- Lee, S. H. et al. Quantum-spin-liquid states in the two-dimensional kagome antiferromagnets $\text{Zn}_x\text{Cu}_{4-x}(\text{OD})_6\text{Cl}_2$. *Nat. Mater.* **6**, 853–857 (2007).
- Fak, B. et al. Kapellasite: a kagome quantum spin liquid with competing interactions. *Phys. Rev. Lett.* **109**, 037208 (2012).
- Fu, M., Imai, T., Han, T. H. & Lee, Y. S. Evidence for a gapped spin-liquid ground state in a kagome Heisenberg antiferromagnet. *Science* **350**, 655–658 (2015).
- Liu, Q. et al. Electron doping of proposed kagome quantum spin liquid produces localized states in the band gap. *Phys. Rev. Lett.* **121**, 186402 (2018).
- Zhao, H. et al. Cascade of correlated electron states in the kagome superconductor CsV_3Sb_5 . *Nature* **599**, 216–221 (2021).
- Jiang, Y. X. et al. Unconventional chiral charge order in kagome superconductor KV_3Sb_5 . *Nat. Mater.* **20**, 1353–1357 (2021).
- Li, H. et al. Rotation symmetry breaking in the normal state of a kagome superconductor KV_3Sb_5 . *Nat. Phys.* **18**, 265–270 (2022).
- Teng, X. et al. Magnetism and charge density wave order in kagome FeGe. *Nat. Phys.* **19**, 814–822 (2023).
- Ortiz, B. R. et al. CsV_3Sb_5 : A Z_2 topological kagome metal with a superconducting ground state. *Phys. Rev. Lett.* **125**, 247002 (2020).
- Ortiz, B. R. et al. Superconductivity in the Z_2 kagome metal KV_3Sb_5 . *Phys. Rev. Mater.* **5**, 034801 (2021).
- Nie, L. et al. Charge-density-wave-driven electronic nematicity in a kagome superconductor. *Nature* **604**, 59–64 (2022).
- Sun, K., Souslov, A., Mao, X. & Lubensky, T. C. Surface phonons, elastic response, and conformal invariance in twisted kagome lattices. *Proc. Natl Acad. Sci. USA* **109**, 12369–12374 (2012).
- Zhang, S. et al. Kagome bands disguised in a coloring-triangle lattice. *Phys. Rev. B* **99**, 100404 (2019).
- Duran, A. C., Osorio, S. A. & Sturla, M. B. Anomalous hall effect in the coplanar antiferromagnetic coloring-triangular lattice. *Phys. Rev. B* **106**, 045101 (2022).
- Liu, H., Meng, S. & Liu, F. Screening two-dimensional materials with topological flat bands. *Phys. Rev. Mater.* **5**, 084203 (2021).
- Gao, Y. et al. Quantum anomalous hall effect in two-dimensional Cu-dicyanobenzene coloring-triangle lattice. *Nano Res.* **13**, 1571–1575 (2020).
- Lei, L. et al. Electronic Janus lattice and kagome-like bands in coloring-triangular MoTe_2 monolayers. *Nat. Commun.* **14**, 6320 (2023).
- Dong, H. et al. Emergent electronic kagome lattice in correlated charge-density-wave state of 1T-TaS₂. Preprint at <https://arxiv.org/abs/2301.05885> (2023).
- Zhang, Y. et al. Ultrathin magnetic 2D single-crystal CrSe. *Adv. Mater.* **31**, e1900056 (2019).
- Li, B. et al. Van der Waals epitaxial growth of air-stable CrSe_2 nanosheets with thickness-tunable magnetic order. *Nat. Mater.* **20**, 818–825 (2021).
- Liu, M. et al. Diverse structures and magnetic properties in non-layered monolayer chromium selenide. *J. Phys. Chem. Lett.* **12**, 7752–7760 (2021).
- Zhu, X. et al. Spin glass state in chemical vapor-deposited crystalline Cr_2Se_3 nanosheets. *Chem. Mater.* **33**, 3851–3858 (2021).
- Gou, J. et al. Binary two-dimensional honeycomb lattice with strong spin-orbit coupling and electron-hole asymmetry. *Phys. Rev. Lett.* **121**, 126801 (2018).
- Wang, Q. et al. Large-scale uniform bilayer graphene prepared by vacuum graphitization of 6H-SiC(0001) substrates. *J. Phys. Condens* **25**, 095002 (2013).

Acknowledgements

This work was supported by the Natural Science Foundation of China (62274118, W.C.), Singapore National Research Foundation Investigatorship Program under Grant No. NRF NRF108-2022-0009 (W.C.), SUSTech-NUS Joint Research Program, Singapore MOE Grants of MOE-T2EP50220-0001 (W.C.), MOE2018-T3-1-002 (C.Z.), MOE WBS A-8000942-00-00 (A.T.S.W.), and the Science and Engineering Research Council of A*STAR (Agency for Science, Technology and Research) Singapore under Grant No. A20G9b0135 (W.C.), Beijing Natural Science Foundation (JQ23001, B.F.), the International Partnership Program of Chinese Academy of Sciences (112111KYSB20200012, B.F.), the Strategic Priority Research Program of Chinese Academy of Sciences (XDB33030100, B.F.), and the CAS Project for Young Scientists in Basic Research (YSBR-047, B.F.). Y.L.H. acknowledges financial support from the National Natural Science Foundation of China (Grant No.12350610236, Y.L.H.) and the Natural Science Foundation of Fujian Province (2022J06035, Y.L.H.). The authors would like to acknowledge Y.Xu. and L.Jiao for the fruitful discussion and the Singapore Synchrotron Light Source for providing the facility necessary for conducting the research. The laboratory is a National Research Infrastructure under the National Research Foundation, Singapore. Any opinions, findings and conclusions or recommendations expressed in this material are those of the author(s) and do not reflect the views of National Research Foundation, Singapore.

Author contributions

S.D., J.-Y.Y., Z.C., and J.G. contributed equally to this work. W.C., J.G., and A.T.S.W. conceived the idea and designed the research. S.D., J.G., and Y.L.H. contributed to the sample preparation. S.D. and J.G. performed STM/STS and nc-AFM measurements. S.D., J.G., Y.L.H., S.S., and Y.W. contributed to the development and maintenance of the STM/nc-AFM system. J.-Y.Y. and C. Z. performed the theoretical analysis. Z.C., D.L., and B.F. performed ARPES measurements. M.L. and S.L.T. performed the cross-sectional STEM characterization. X.Y. performed the XMCD characterization. S.D., J.G., J.-Y.Y., and Z.C. analyzed the experimental data and wrote this paper with comments from all authors.

Competing interests

The authors declare no competing interests.

Additional information

Supplementary information The online version contains supplementary material available at <https://doi.org/10.1038/s41467-024-53314-1>.

Correspondence and requests for materials should be addressed to Jian Gou, Ming Lin, Baojie Feng, Andrew T. S. Wee or Wei Chen.

Peer review information *Nature Communications* thanks Dongwook Kim, and the other, anonymous, reviewer(s) for their contribution to the peer review of this work. A peer review file is available.

Reprints and permissions information is available at <http://www.nature.com/reprints>

Publisher's note Springer Nature remains neutral with regard to jurisdictional claims in published maps and institutional affiliations.

Open Access This article is licensed under a Creative Commons Attribution-NonCommercial-NoDerivatives 4.0 International License, which permits any non-commercial use, sharing, distribution and reproduction in any medium or format, as long as you give appropriate credit to the original author(s) and the source, provide a link to the Creative Commons licence, and indicate if you modified the licensed material. You do not have permission under this licence to share adapted material derived from this article or parts of it. The images or other third party material in this article are included in the article's Creative Commons licence, unless indicated otherwise in a credit line to the material. If material is not included in the article's Creative Commons licence and your intended use is not permitted by statutory regulation or exceeds the permitted use, you will need to obtain permission directly from the copyright holder. To view a copy of this licence, visit <http://creativecommons.org/licenses/by-nc-nd/4.0/>.

© The Author(s) 2024